Nano Research

Open Access

Research Article

Strontium carbonate: A bifunctional support to enhance Ru catalysts for ammonia synthesis under mild conditions

Xiaohu Hu[1,§], Jiakai Wang[1,§], Zhongliang Cao[1,§], Haolong Chang[1], Yifan Yan[1], Zhenjie Sun[1], Xing Chen[1,2], Langli Luo[1,2], and Yongan Yang[1,2] ✉

[1] *Institute of Molecular Plus, Department of Chemistry, School of Chemical Engineering and Technology, National Industry-Education Platform for Energy Storage, Tianjin University, Tianjin 300072, China*
[2] *Haihe Laboratory of Sustainable Chemical Transformations, Tianjin 300192, China*
[§] *Xiaohu Hu, Jiakai Wang, and Zhongliang Cao contributed equally to this work.*

Cite this article: *Nano Research*, **2026**, *19*, 94908744. https://doi.org/10.26599/NR.2026.94908744

ABSTRACT: Toward enhancing the NH_3 synthesis activity of Ru-based catalysts under mild conditions, various electron donors have been intensively investigated. The electron donation typically originates from either the support itself or the external promoter that transforms into a near-metallic state during the reaction, yet single materials combining both pathways remain rarely reported. This work developed such a bifunctional support, strontium carbonate ($SrCO_3$). Over the Ru-$SrCO_3$/carbon nanotubes (CNTs) catalyst, surface $SrCO_3$ was partially reduced *in-situ* to form near-metallic Sr^0 species, which, together with the unreduced basic Sr^{2+} in the bulk $SrCO_3$, donate electrons to Ru sites, achieving highly efficient N_2 activation. Moreover, the $SrCO_3$ support can also boost NH_3 desorption and mitigate hydrogen poisoning. The potassium-promoted catalyst K-Ru-$SrCO_3$/CNTs even delivers an outstanding NH_3-synthesis rate of 61.6 $mmol_{NH_3} \cdot g_{cat}^{-1} \cdot h^{-1}$ at 400 °C and 0.9 MPa, outperforming most state-of-the-art Ru-based catalysts with Ru mass-loading ≤ 5 wt.% reported to date.

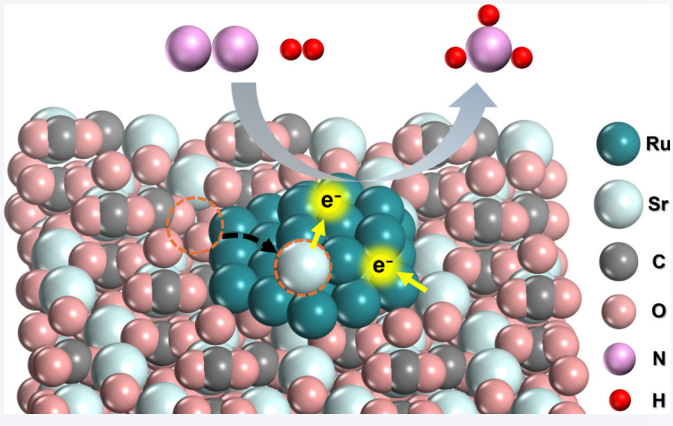

KEYWORDS: ammonia synthesis, Ru-based catalysts, strontium carbonate, electron donation

1 Introduction

The world has experienced multiple times of fossil fuels-related energy crises since the 21st century [1, 2]. Toward establishing the sustainable development, carbon-free fuels will play the pivotal role, as they not only reduce carbon emissions but also promote renewable energies [3, 4]. Building on this, the strategic value of hydrogen energy, particularly "green hydrogen" produced via water electrolysis using renewable electricity, has become increasingly prominent [5–7]. However, significant challenges still remain in achieving economical, efficient, and large-scale supply of pure hydrogen [8, 9]. Recently, ammonia (NH_3) has been widely recognized as an ideal hydrogen carrier due to its superior hydrogen content (17.6 wt.%), ease of storage, and excellent safety [10, 11]. Moreover, as a zero-carbon fuel with a relatively high mass energy density (3 $kWh \cdot g^{-1}$), NH_3 itself is regarded as a promising new energy source [12, 13]. At present, the dominant method for industrial NH_3 synthesis is the century-old Haber–Bosch (HB) process, which catalyzes the reaction of N_2 with H_2 at high temperatures (450–500 °C) and high pressures (15–20 MPa) over iron-based catalysts [14]. A major bottleneck of this process is its heavy reliance on fossil fuels, which leads to substantial carbon emissions (~ 1.5 tons of CO_2 per ton of NH_3) [15]. The electrolysis-driven HB process (eHB) has thus emerged as a promising pathway for green NH_3 synthesis, aligning with the global pursuit of carbon neutrality and the rising demand for clean energies [16]. However, a challenge arises from the pressure discrepancy: The hydrogen output from water electrolysis is typically below 5 MPa, which is significantly lower than the pressure in the conventional Fe-catalyzed HB process. This mismatch underscores the importance of developing catalysts capable of efficient NH_3 synthesis at low pressures and low temperatures. In this regard, Ru-based catalysts

Received: February 5, 2026; **Revised:** March 25, 2026
Accepted: April 17, 2026

✉Address correspondence to revned_yang@tju.edu.cn

offer a promising advantage, as they exhibit superior intrinsic activity under mild conditions compared to traditional Fe-based catalysts, thereby potentially meeting the required performance benchmarks.

For further improving the NH_3 synthesis activity of Ru-based catalysts, the efficient activation of N_2 molecule is critical, which is challenging due to the high bond energy of N≡N (941 kJ·mol^{-1}) [17]. It is well established that N_2 cleavage can be significantly promoted by electron donation from an electron-rich catalyst into the antibonding π^* orbital of N_2 molecule via the d-orbitals of Ru metal [18, 19]. Such electron-rich materials, including the functional supports themselves and externally added promoters, have been extensively studied for Ru-based catalysts. For example, Ru/Ca_2N:e^- [20], Ru/C12A7:e^- [21], and Ru/CaFH [22] catalysts employ supports with exceptionally strong electron-donating capabilities, which lead to significant NH_3 synthesis rates; 5K-Ru/MgO nanoclusters enable high catalytic activity, owing to the K addition that optimizes the electronic structure of the Ru active sites [23]. Ru(10%)/C_inCs, which means Ru catalysts *in-situ* doped with metallic Cs promoter, exhibits one of the best performance ever reported [24]. In the studies mentioned above, the electron-donating effect is typically achieved either through the compound supports themselves or via externally added promoters that convert to a near-metallic state during reaction [25, 26]. Nevertheless, there are few (if any) reports on a single material capable of both pathways with the exception of the Co/LaN system, wherein the surface LaN is partially reduced *in-situ* to metallic La, which migrates onto Co clusters and thereby promotes N_2 activation [27]. Integrating both electron-donating pathways within a single material can synergistically enhance the ability of Ru to activate N_2, while also improving the utilization efficiency of all catalyst components. These combined advantages are crucial for developing highly efficient Ru-based NH_3 synthesis catalysts that operate under mild conditions and are promising for industrial applications.

In fact, the bifunctional support that integrates the two electron-donating pathways essentially combines the functions of both a support and a promoter. Among alkaline earth metals (AEMs), there seems a clear trend: The light AEM-based oxide MgO is primarily employed as high-surface-area support [28, 29] and CaO is commonly used as a reference support in studies [21, 30], whereas the heavy AEM-based oxide BaO is widely recognized as a potent structural promoter that enhances the N_2 dissociation rate [31–33]. This trend suggests a scientific hypothesis: Strontium (Sr), positioned between Ca and Ba, might possess the unique capability to serve as a bifunctional support that provides both support and promoter functionalities. However, SrO has not been documented, while there are a few studies on other strontium compounds-based catalysts including Co/SrNH [34], Ru/$Sr_2Ta_2O_7$ [35], and Ru/$SrTiO_3$ [36]. Additionally, the practical application of SrO is hindered by its strong hygroscopicity. Then, the exploration of bifunctional catalyst supports can proceed along the line of strontium compounds. A recent study [37] revealed that $BaCO_3$, which is converted from the $Ba(NO_3)_2$ precursor, acts as an effective promoter species under reaction conditions. This report inspires us to hypothesize that $SrCO_3$ might be a bifunctional catalyst support.

Therefore, this study focuses on the Ru/$SrCO_3$ catalyst. It demonstrates a NH_3 synthesis rate of 2.5 $mmol_{NH_3}·g_{cat}^{-1}·h^{-1}$ at 400 °C and 0.1 MPa, 18 times that of Ru/carbon nanotubes (CNTs), whose support serves only for the metal dispersion. In the Ru/$SrCO_3$ system, $SrCO_3$ itself acts as an alkaline support and facilitates electron donation to Ru in the form of a compound [37]. To enhance the catalytic performance, CNTs were employed to support both Ru and $SrCO_3$, producing Ru-$SrCO_3$/CNTs, a choice motivated by its high specific surface area and abundant anchoring sites that facilitate high dispersion of Ru and $SrCO_3$ particles [38]. Therein $SrCO_3$ is predominantly anchored around Ru nanoparticles, due to a strong metal–support interaction (SMSI) between Ru and $SrCO_3$ [39]. Notably, near-metallic Sr species (Sr^0) are generated by the reduction of surface $SrCO_3$ under the reaction conditions over Ru-$SrCO_3$/CNTs, which plays a more important role in enhancing the electron-rich state of the Ru entities. The formation of Sr^0 is likely attributable to the dual reduction of surface $SrCO_3$ by active H species and carbon [40], indicating that the CNTs serve both to disperse Ru metal and to reduce the surface $SrCO_3$. Within this system, two distinct electron-donation pathways are concurrently facilitated by the $SrCO_3$ support, leading to a remarkably enhanced NH_3 synthesis rate of 3.0 $mmol_{NH_3}·g_{cat}^{-1}·h^{-1}$. To further boost the catalyst performance, the potassium promotor, which is a commonly-employed electron promoter due to its strong capability of donating electrons to Ru [23, 41, 42], was utilized to make a composite catalyst K-Ru-$SrCO_3$/CNTs. With K addition, K-Ru-$SrCO_3$/CNTs present an extraordinary NH_3-synthesis rate of 61.6 $mmol_{NH_3}·g_{cat}^{-1}·h^{-1}$ at 400 °C and 0.9 MPa, which not only surpasses most state-of-the-art Ru-based catalysts with Ru mass-loading ≤ 5 wt.%, but also demonstrates sustained durability for more than 100 h.

2 Experimental

2.1 Materials

$Sr(NO_3)_2$ (≥ 99.5%) was purchased from Tianjin Damao chemicals reagent factory. Na_2CO_3 (≥ 98%) and $Ru_3(CO)_{12}$ (≥ 99%) were bought from Shanghai Aladdin Biochemical Technology. CNTs (surface area > 120 $m^2·g^{-1}$) were purchased from Shenzhen Co., Ltd. WO_3 (≥ 99%) and $KHCO_3$ (≥ 99.99%) were purchased from Macklin Co., Ltd. N_2 (99.999%), H_2 (99.999%), Ar (99.999%), CO (99.999%), and N_2/H_2 mixtures with different molar ratios (99.999%) were obtained from Tianjin Air Liquide Gases.

2.2 Synthesis of $SrCO_3$ support

Two series of solutions for $Sr(NO_3)_2$ and Na_2CO_3 with fixed molar ratio of 1:1 between them were respectively prepared at several concentrations of 0.5%, 1%, 2%, 5%, and saturation. Then the Na_2CO_3 solution was added dropwise (2 mL·min^{-1}) into the $Sr(NO_3)_2$ solution under continuous sonication at room temperature. After the reaction was complete, the suspension mixture was filtered. The collected white powder was washed thoroughly with water and then dried at 80 °C for 12 h to obtain the $SrCO_3$ support. As shown in Fig. S1 in the Electronic Supplementary Material (ESM), all X-ray diffraction (XRD) peaks of the obtained sample could be assigned to $SrCO_3$ (JCPDS No. 01-084-1778), confirming the successful synthesis of a pure crystalline phase of $SrCO_3$. Additionally, the strongest diffraction peak at 2θ of 25.3° corresponded to the (111) facet. As for the specific surface area derived from N_2 physical adsorption (Fig. S2 in the ESM), $SrCO_3$ synthesized from saturated solutions of $Sr(NO_3)_2$ and Na_2CO_3 possessed the largest specific surface area of 6.1 $m^2·g^{-1}$, which was used for the subsequent catalysts preparation.

2.3 Synthesis of $SrCO_3$/CNTs support

$SrCO_3$ synthesized from saturated solutions of precursors was supported on CNTs via ball milling with a $SrCO_3$-to-CNTs mass ratio of 9:1, 8:2, and 6:4, producing $SrCO_3$/CNTs composite supports. XRD patterns and N_2 physical adsorption results of pure CNTs and these three composite supports are shown in Figs. S3–S5 in the ESM.

2.4 Preparation of Ru-based catalysts

Ru/CNTs, Ru/$SrCO_3$, and Ru-$SrCO_3$/CNTs catalysts were prepared by a one-step solid grinding procedure. Specifically, 0.018 g of $Ru_3(CO)_{12}$ and 0.200 g of the corresponding support were mixed thoroughly by a mortar and pestle. The resulting homogeneous mixture of $Ru_3(CO)_{12}$ and supports obtained via grinding for 15 min was then heated under a 25%N_2-75%H_2 flow at 400 °C for 2 h, producing Ru/CNTs, Ru/$SrCO_3$, and Ru-$SrCO_3$/CNTs catalysts. Additionally, the Ru contents and the corresponding error range determined by inductively coupled plasma optical emission spectroscopy (ICP-OES) analysis of these catalysts are presented in Table S1 in the ESM.

2.5 Preparation of K-promoted Ru-based catalysts

The as-prepared Ru-based catalysts in Section 2.4 was thoroughly mixed with 0.028 g of $KHCO_3$ via grinding for 15 min in an agate mortar. The resulted powder was subsequently heated under a 25%N_2-75%H_2 flow at 400 °C for 2 h, producing K-Ru/CNTs, K-Ru/$SrCO_3$, and K-Ru-$SrCO_3$/CNTs catalysts. The K and Ru contents and the corresponding error range determined by ICP-OES analysis of these catalysts are presented in Table S1 in the ESM.

2.6 NH_3 synthesis performance tests

First, the catalyst powder was pelletized, manually crushed, and finally sieved with a 20–40 mesh. The obtained catalyst grains were then diluted with a proportionate amount of quartz sand to achieve a consistent volume of 1 mL. Finally, the catalyst sample was loaded into a pressurized fixed-bed reactor made of stainless steel for catalytic tests of NH_3 synthesis. The NH_3 synthesis rates over the as-prepared catalysts were evaluated at a feed composition of 40%N_2-60%H_2 with a weight hourly space velocity (WHSV) of 48,000 mL·g^{-1}·h^{-1} at 0.1 MPa and a feed composition of 67%N_2-33%H_2 with a WHSV of 96,000 mL·g^{-1}·h^{-1} at 0.9 MPa. The gas ratio of N_2:H_2 = 2:3 was chosen for investigating the NH_3 synthesis performance, since the study on the effect of N_2:H_2 ratio revealed that this ratio exhibits the highest NH_3-synthesis rate among the N_2:H_2 ratios ranging from 1:3 to 3:1 (Fig. S6 in the ESM). This result is understandable since N_2 activation is the rate-determining step on Ru and a higher N_2 partial pressure compared to the stoichiometric ratio (25%) can effectively enhance the surface reaction rate. To determine the NH_3 formation rate at each condition, the gaseous NH_3 was absorbed by an aqueous solution of 7.5 mM H_2SO_4. The amount of NH_4^+ was assessed by an ion chromatography (Metrohm, ECO IC). Note that the preparation of Ru-$SrCO_3$/CNTs and K-Ru-$SrCO_3$/CNTs utilized the $SrCO_3$-to-CNTs mass ratio of 8:2, which exhibited the highest activity (Fig. S7 in the ESM). Furthermore, the apparent activation energy (E_a) values of the working catalysts were determined from the slopes of Arrhenius plots constructed from the NH_3 synthesis rates measured between 340 and 370 °C at 0.1 MPa.

2.7 Measurement of reaction orders

Ammonia synthesis rate (r) can be given by the following equation [43]

$$r = kP_{N_2}^{\alpha}P_{H_2}^{\beta}P_{NH_3}^{\gamma} \quad (1)$$

where k denotes the reaction rate constant, P_{N_2}, P_{H_2}, and P_{NH_3} are the partial pressures of N_2, H_2, and NH_3, respectively, and α, β, and γ represent the reaction orders for N_2, H_2, and NH_3, respectively. The volumetric fractions of the feed gases containing N_2, H_2, and Ar were varied for determining the reaction orders of N_2 and H_2, as summarized below: (12.5%, 37.5%, 50%), (25%, 37.5%, 37.5%), (35%, 37.5%, 27.5%), (45%, 37.5%, 17.5%), (55%, 37.5%, 7.5%), and (62.5%, 37.5%, 0%) for N_2 reaction orders, likewise (25%, 62.5%, 12.5%), (25%, 50%, 25%), (25%, 37.5%, 37.5%), (25%, 25%, 50%), and (25%, 12.5%, 62.5%) for H_2 reaction orders. The NH_3 reaction orders were measured by varying the 40%N_2-60%H_2 flow rate from 15 o 60 mL·min^{-1}. All kinetic results (reaction orders and activation energies) were obtained well below the equilibrium states. The specific calculation method followed the procedures described in Ref. [23].

2.8 Catalyst characterizations

XRD was conducted to identify the crystalline phases of catalysts on a Rigaku Smartlab 9KW diffractometer using Cu Kα radiation (λ = 0.15406 nm). N_2 physical adsorption was conducted on an ASAP 2020 apparatus to determine the Brunauer–Emmett–Teller (BET) surface area of catalysts. Inductively coupled plasma optical emission spectroscopy (ICP-OES) measurements were conducted on an Agilent 5110 (OES) spectrometer to measure the K and Ru contents of the catalysts. The morphologies of the catalysts were characterized by scanning electron microscopy (SEM, FEI Apreo S LoVac, Czech Republic) and transmission electron microscopy (TEM, Talos F200X field emission transmission electron microscope). The microscope was equipped with a Super-X G2 energy-dispersive X-ray (EDX) spectroscopy detector for elemental analysis. X-ray photoelectron spectroscopy (XPS) and ultraviolet photoelectron spectroscopy (UPS) measurements were performed to investigate the electronic structure of catalysts using a Thermo Fisher Scientific Escalab 250Xi photoelectron spectrometer equipped with a monochromatic Al Kα source (1486.6 eV). The calibration of all XPS binding energies was performed using the C 1s signal of adventitious carbon at 284.8 eV as the standard reference. The full width at half maximum (FWHM) values for Ru^0 and $Ru^{\gamma+}$ were 3.50 eV for all systems. For quasi *in-situ* XPS, the sample preparation was identical to conventional XPS, but the measurement procedures were different. Prior to testing, the sample was first transferred under vacuum to an *in-situ* reaction cell, where it was then sequentially treated at 400 °C in Ar, H_2, N_2, and finally a 25%N_2-75%H_2 mixture. After each treatment, the catalyst was transferred back to the analysis chamber for characterization. The WO_3 color change experiments were performed by mixing each catalyst evenly with pure WO_3 powder at a mass ratio of 1:80. The obtained mixture was first heated to 200 °C under an Ar flow. The gas was then switched to pure H_2, and the color of the mixture was recorded after reduction for 0, 2, 5, and 15 min, respectively. *In-situ* diffuse reflectance infrared Fourier transform spectroscopy (DRIFTS) was conducted on a Bruker INVENIO S spectrometer in the range of 700–4000 cm^{-1}. The *in-situ* DRIFTS spectra for N_2 and CO were collected at 300 and 50 °C, respectively.

2.9 Theoretical simulation

All calculations were performed using the density functional theory (DFT) method with the projector augmented wave (PAW) as implemented in the Vienna *ab initio* simulation package (VASP, version 5.4.4) [44–46]. The generalized gradient approximation (GGA) of the Perdew–Burke–Ernzerhof (PBE) functional was adopted to deal with the exchange–correlation interactions [47, 48]. The cut-off energy of the plane-wave basis set was 550 eV and 2 × 1 × 1 gamma-point sampling was used for Brillouin zone integration. The energy and force convergence criterions for geometry optimization were 1×10^{-5} eV and −0.05 eV·Å^{-1}, respectively.

3 Results and discussion

3.1 Performance

As displayed in Fig. 1(a), pure $SrCO_3$ shows no measurable activity for NH_3 synthesis at 400 °C and 0.1 MPa. Upon Ru loading, the Ru/$SrCO_3$ catalyst exhibits a relatively high rate of 2.5 $mmol_{NH_3}·g_{cat}^{-1}·h^{-1}$, indicating Ru is the major active site. Moreover, to understand the N_2 dissociation process, the rate-determining step for NH_3 synthesis as revealed by the N_2 reaction order (explained later), DFT calculations were employed to compare the N_2-adsorption over $SrCO_3$ and Ru/$SrCO_3$ (Fig. S8 in the ESM). The $SrCO_3$ support exhibits negligible N_2 adsorption, with an adsorption energy of only −0.08 eV. In contrast, the adsorption energy of N_2 on Ru/$SrCO_3$ increases to −0.30 eV, indicating significantly enhanced N_2 adsorption. Meanwhile, the N≡N bond length increases from 1.11 to 1.31 Å. These computational results underscore the indispensable role of Ru in the adsorption and activation of N_2, key steps for NH_3 synthesis. Besides, the NH_3 synthesis rate of Ru/$SrCO_3$ is 18-fold that of Ru/CNTs (0.14 $mmol_{NH_3}·g_{cat}^{-1}·h^{-1}$), indicating the significant improvement of NH_3 synthesis performance over Ru/$SrCO_3$. When increasing the reaction pressure to 0.9 MPa, the NH_3 synthesis rate of Ru/$SrCO_3$ reaches 13.5 $mmol_{NH_3}·g_{cat}^{-1}·h^{-1}$, suggesting that further enhancement of the NH_3 synthesis rate over Ru/$SrCO_3$ can be achieved by reaction engineering optimization.

Although the direct catalytic contribution of CNTs is limited, they have emerged as promising support components for Ru-based NH_3 synthesis due to their positive impact lying in high surface area, tunable surface functional groups, and exceptional electrical conductivity [38, 49, 50]. In our case, their high specific surface area (120.7 $m^2·g^{-1}$, Fig. S5 in the ESM) provides an effective route to disperse Ru/$SrCO_3$ that presents a comparatively low surface area (6.1 $m^2·g^{-1}$, Fig. S2 in the ESM). Accordingly, a series of $SrCO_3$/CNTs composite supports was prepared via ball milling. By maintaining a $SrCO_3$-to-CNTs mass ratio of 4:1 ($m_{SrCO_3}/m_{CNTs} = 4$), the target composite $SrCO_3$/CNTs was obtained. With the addition of CNTs, the specific surface area of the composite support increased to 38.1 $m^2·g^{-1}$, which is 6.2-fold that of pure $SrCO_3$ (Fig. S9 in the ESM). Upon Ru loading, Ru-$SrCO_3$/CNTs exhibits an optimal NH_3 synthesis activity at 400 °C and 0.9 MPa (14.3 $mmol_{NH_3}·g_{cat}^{-1}·h^{-1}$).

Furthermore, the addition of alkali or alkaline earth metal promoters can significantly enhance the catalytic activity of active metals. In Ru-based NH_3 synthesis catalysts, the activity-enhancing mechanisms of these promoters have traditionally been classified as either electronic or structural effects. Alkali metals-based promotors (e.g., Cs and K) are generally employed by utilizing their enhanced back donation of electrons to the antibonding orbitals of N_2 molecules to assist the N≡N bond dissociation [41, 51]. In addition, the electrostatic interaction also plays an important role in

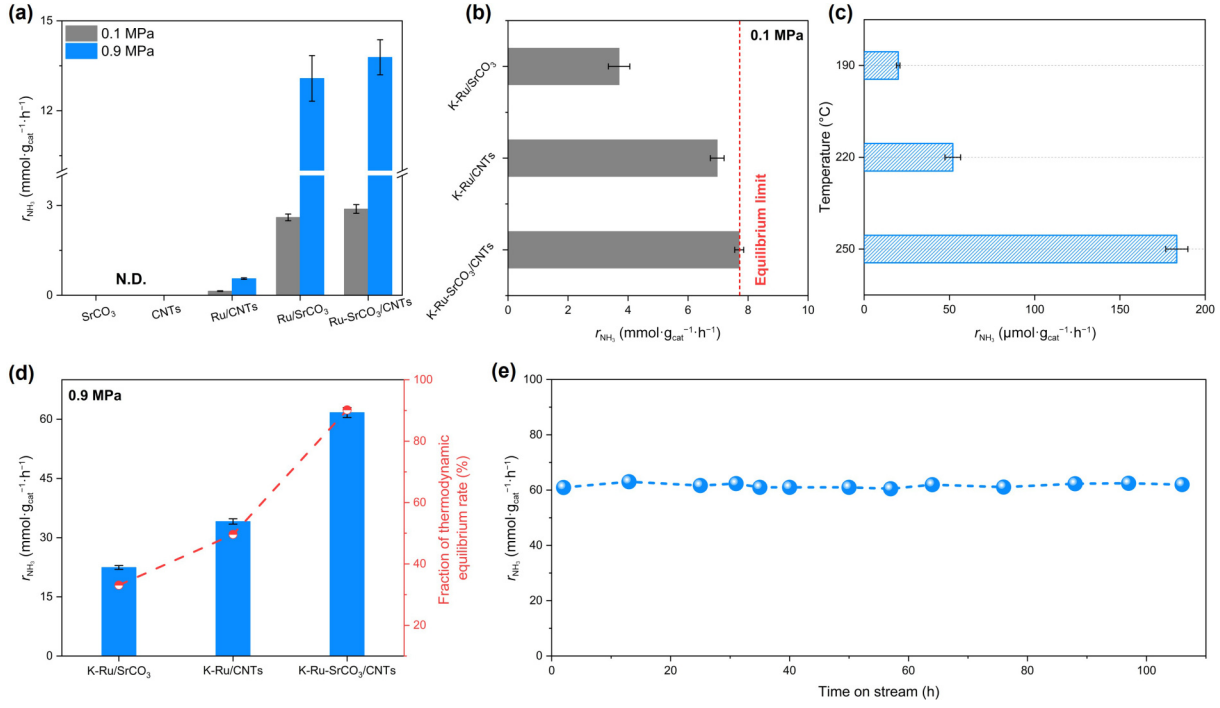

Figure 1 Catalytic performance. (a) NH_3 synthesis rates over the as-prepared catalysts at 400 °C under 0.1 and 0.9 MPa. (b) NH_3 synthesis rates over the K-promoted catalysts at 400 °C and 0.1 MPa. (c) NH_3 synthesis rates of K-Ru-$SrCO_3$/CNTs at 190–250 °C and 0.1 MPa. (d) NH_3 synthesis rates over the K-promoted catalysts at 400 °C and 0.9 MPa. The error bars represent the standard deviation based on three independent catalytic tests performed under the stated conditions. (e) Catalytic stability of K-Ru-$SrCO_3$/CNTs catalysts at 400 °C and 0.9 MPa.

promoting NH_3 synthesis. For instance, the introduction of Li^+ over Ru/AC catalysts significantly polarizes and stabilizes the adsorbed dinitrogen intermediates on terrace sites, greatly facilitating NH_3 synthesis [25]. Besides the electronic effect, Ba also behaves as a structural promoter (such as in the form of BaO_x) to reduce the sintering of Ru [52]. In the process of understanding the mechanistic roles of promoters, traditional *ex situ* characterizations often fail to capture the dynamic chemical states and spatial distribution of promoters under realistic working conditions. Recent advancements of *in-situ* and *operando* characterization techniques have provided transformative insights, allowing direct tracking of promoter evolution under reaction conditions [53]. For example, using *in-situ* environmental transmission electron microscopy (ETEM), Hansen et al. investigated the structural evolution of Ba-promoted Ru catalysts under NH_3 synthesis conditions. They found that Ba species did not uniformly cover the Ru surface but instead existed as an amorphous oxygen-containing adlayer on specific facets of Ru, and were able to migrate during the reaction [54]. This finding directly demonstrates that Ba plays the major role of a structural promoter rather than an electronic promoter. Furthermore, with one of the best performances ever reported [24], Ru(10%)/C_inCs suggests that alkali metal promoters are most effective when reduced to the metallic state during the reaction, a conclusion consistent with DFT calculations [55]. Collectively, these *operando* observations highlight the critical role of promoters in NH_3 synthesis. On this basis, K, known to function as an electron promoter [56], was introduced into the Ru/CNTs, Ru/$SrCO_3$, and Ru-$SrCO_3$/CNTs catalysts (Fig. 1(b)).

At 400 °C and 0.1 MPa, the NH_3-synthesis rates of these three K-promoted catalysts range from 3.9 to 7.7 $mmol_{NH_3} \cdot g_{cat}^{-1} \cdot h^{-1}$. Specifically, the addition of K promoter increases the NH_3-synthesis rate of Ru-$SrCO_3$/CNTs by a factor of 2.6 (from 3.0 to 7.7 $mmol_{NH_3} \cdot g_{cat}^{-1} \cdot h^{-1}$). This promotional effect can be attributed to the electron-donating role of K, as evidenced by the Ru 3p XPS spectra (Fig. S10 in the ESM): The binding energy of Ru^0 decreases from 462.0 (Ru-$SrCO_3$/CNTs) to 461.8 eV (K-Ru-$SrCO_3$/CNTs), indicating increased electron density on the Ru surface upon K addition. Notably, the K-Ru-$SrCO_3$/CNTs catalyst achieves an NH_3 concentration of 0.40 vol.%, which reaches the thermodynamic equilibrium under the given conditions. Consequently, under 0.1 MPa, the NH_3 synthesis rates of K-Ru-$SrCO_3$/CNTs reach up to 8.8 and 8.6 $mmol_{NH_3} \cdot g_{cat}^{-1} \cdot h^{-1}$ at 390 and 380 °C, respectively (Fig. S11 in the ESM), which are both higher than that of 400 °C (7.7 $mmol_{NH_3} \cdot g_{cat}^{-1} \cdot h^{-1}$). In addition, the NH_3 synthesis was even operative at ≤ 250 °C and 0.1 MPa over K-Ru-$SrCO_3$/CNTs (Fig. 1(c)). Furthermore, K-Ru-$SrCO_3$/CNTs delivers a NH_3-synthesis rate of 61.6 $mmol_{NH_3} \cdot g_{cat}^{-1} \cdot h^{-1}$ at 400 °C and 0.9 MPa (Fig. 1(d)), which is one of the best catalysts with Ru mass-loading ≤ 5 wt.% ever reported (Table S2 in the ESM). Evidently, the activity of K-Ru-$SrCO_3$/CNTs catalysts also outperforms most previously reported oxide- and carbon-supported Ru catalysts (Table S3 in the ESM). While some catalysts with high Ru loadings (4.5 wt.%–10 wt.%) show higher absolute rates, our catalyst exhibits superior mass-specific activity among those with low Ru content (≤ 3.0 wt.%). The exploration of $SrCO_3$ provides a novel strategy for NH_3 synthesis beyond traditional supports. However, optimizing activity for a new system demands greater effort and time, as key factors, promoter type, loading, and addition method, cannot be directly transferred from established oxide- or carbon-supported Ru-based catalysts. Moreover, the NH_3-synthesis rate of K-Ru-$SrCO_3$/CNTs accounts for 90% of the thermodynamic equilibrium and is 1.8-fold that of K-Ru/CNTs (33.9 $mmol_{NH_3} \cdot g_{cat}^{-1} \cdot h^{-1}$), highlighting the essential role of $SrCO_3$ in improving NH_3 synthesis performance over Ru-based catalysts. Additionally, the best-performing catalyst K-Ru-$SrCO_3$/CNTs maintained constant activity without observable deactivation for 105 h at 400 °C and 0.9 MPa (Fig. 1(e)), demonstrating its high stability.

3.2 Kinetics

To probe the functions of $SrCO_3$ over the catalysts, kinetic analyses were performed and the results are presented in Fig. 2. As shown in the Arrhenius plots (Fig. 2(a)), the K-Ru-$SrCO_3$/CNTs catalyst exhibits the lowest apparent activation energy (E_a = 66 kJ·mol^{-1}) among the tested catalysts (K-Ru/$SrCO_3$, K-Ru/CNTs, and K-Ru-$SrCO_3$/CNTs). This lowest E_a reflects the enhanced activation of N_2 and H_2, resulting in the highest NH_3 synthesis rate. As a product, NH_3 is expected to present a negative reaction order, as a higher concentration will lead to a lower reaction rate. Among the K-promoted catalysts, the NH_3 reaction orders $\gamma(NH_3)$ were less negative over the $SrCO_3$-supported catalysts (e.g., −0.66 for K-Ru-$SrCO_3$/CNTs and −0.70 for K-Ru/$SrCO_3$) than that on K-Ru/CNTs (−0.73), indicating facilitated NH_3 desorption via the addition of $SrCO_3$, which is favorable for NH_3 synthesis (Fig. 2(b)). Notably, the NH_3 reaction order herein over K-Ru-$SrCO_3$/CNTs (−0.66) is also less negative than the values for Ru/C12A7:e^- (−1.00) [21] and Ru/Ca_2N:e^- (−1.03) [20]. This fact suggests that NH_3 desorption is relatively facilitated on the $SrCO_3$-modified interface, preventing the blockage of active sites by the produced NH_3, i.e., a less pronounced NH_3 poisoning effect (Fig. 2(b)).

Besides, the N_2 reaction order $\alpha(N_2)$ serves as an indicator of its activation capability, with the obtained results displayed in Fig. 2(c). It was shown that K-Ru-$SrCO_3$/CNTs catalysts possess a relatively small N_2 reaction order of 0.75, compared to conventional Ru catalysts, e.g., 1.5 for Ru(10%)/C_inCs [24], 1.2 for Ni/LaN [57], and 1.0 for Co/CeN [58]. According to the kinetic models for ammonia synthesis, a lower N_2 order in the range of 0.5–0.8 often correlates with an enhanced electron-donating capability of the support/promoter, which facilitates N_2 cleavage and in turn a high coverage of N atoms on the catalyst surface and eventually promotes the formation of NH_3 [59]. Furthermore, the H_2 reaction order $\beta(H_2)$ holds additional significance for Ru-based catalysts because it quantifies the level of hydrogen poisoning [28]. For most of the conventional Ru-based catalysts, the H_2 reaction order is negative. This fact indicates that excess hydrogen adatoms cover active sites of Ru catalysts and then consequently decrease the overall reaction rate [60]. In contrast, $\beta(H_2)$ for the K-Ru-$SrCO_3$/CNTs is positive at 0.72 (Fig. 2(d)), as opposed to a negative value of −0.27 for the K-Ru/CNTs, suggesting a distinct role of $SrCO_3$ addition in alleviating hydrogen poisoning, i.e., the Ru sites are not over-saturated by H* adatoms. Collectively, the kinetic analyses reveal that $SrCO_3$ contributes to enhanced NH_3 synthesis performance through three key mechanisms: facilitating N_2 activation, effectively avoiding hydrogen poisoning, and accelerating NH_3 desorption. Guided by these findings, subsequent studies were conducted to elucidate the origin of high activity over $SrCO_3$-supported catalysts.

3.3 Structural properties

A series of SEM and TEM images with different resolutions was taken to observe the morphology of the Ru/$SrCO_3$ and Ru-$SrCO_3$/CNTs catalysts, as well as the $SrCO_3$ support (Fig. 3, and Figs. S12, S13, and S16 in the ESM). The $SrCO_3$ support is composed of pebble-like primary particles in size of about 70 nm,

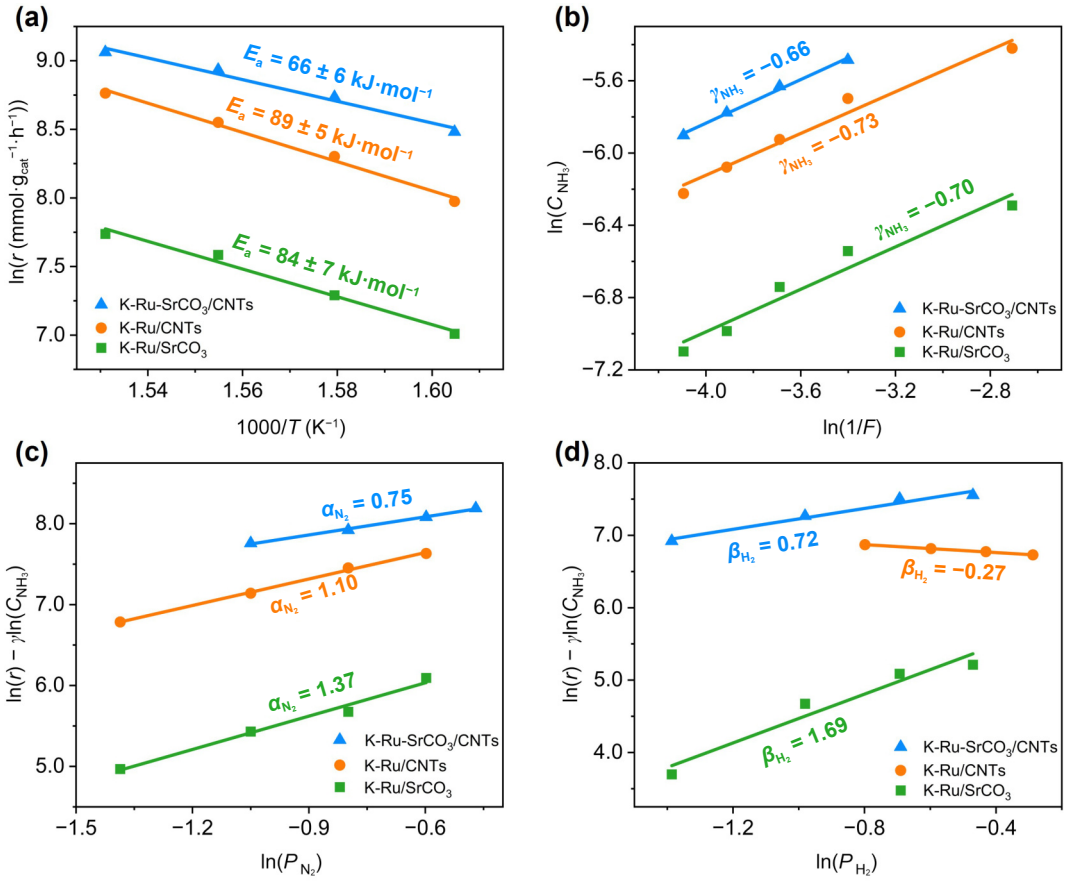

Figure 2 Kinetic analyses. (a) Arrhenius plot of K-Ru/$SrCO_3$, K-Ru/CNTs, and K-Ru-$SrCO_3$/CNTs catalysts at 0.1 MPa. ((b)–(d)) Reaction orders of (b) NH_3, (c) N_2, and (d) H_2 over the K-Ru/$SrCO_3$, K-Ru/CNTs, and K-Ru-$SrCO_3$/CNTs at 370 °C and 0.1 MPa.

with some degrees of particle accumulation (Figs. S12(a)–S12(c) in the ESM). A lattice spacing of 0.350 nm is observed in the $SrCO_3$ support, consistent with the *d*-spacing of its (111) plane (0.352 nm) (Fig. S13 in the ESM). For the Ru/$SrCO_3$ catalyst, XRD patterns of the used Ru/$SrCO_3$ were first analyzed in Fig. S14 in the ESM. Most diffraction peaks can be ascribed to Ru and $SrCO_3$ except few peaks corresponding to $Sr(OH)_2$, a byproduct generated during the XRD sample preparation due to the hydrolysis of Sr^0 species, which were derived from the H_2/CNTs reduction of $SrCO_3$ during the synthetic reaction (explained later). More evidence is provided by the following observations: In the absence of Ru, pure $SrCO_3$ after calcination shows fewer $Sr(OH)_2$ than Ru/$SrCO_3$ (Fig. S15(a) in the ESM); and in the presence of Ru and CNTs, used Ru-$SrCO_3$/CNTs shows more $Sr(OH)_2$/$Sr(OH)_2$·$8H_2O$ than Ru/$SrCO_3$ (Fig. S15(b) in the ESM). Moreover, SEM and TEM results of the used Ru/$SrCO_3$ were presented in Figs. S12(d)–S12(f) and S16 in the ESM. Its particle sizes and shapes are found to be similar with those of the $SrCO_3$ support (Fig. S12(d)–S12(f) in the ESM), but with Ru nanoparticles not observable due to the resolution limit of SEM. The lattice analysis reveals clear fringes of the $SrCO_3$ support with an interplanar spacing of 0.353 nm, matching well with the (111) plane of $SrCO_3$. This fact confirms the predominant exposure of the $SrCO_3$(111) facet, being consistent with the XRD results. The size analysis on Ru nanoparticles indicates an average diameter of 4.3 nm (Fig. S16 in the ESM).

Notably, we also characterized the morphology of the fresh Ru/$SrCO_3$ via high-resolution TEM (HRTEM) and the analysis of Ru particle size distribution is shown in Fig. S17 in the ESM. There is no significant change in Ru particle sizes and size distribution, i.e., 4.1 ± 2.3 nm (before) and 4.3 ± 2.4 nm (after), indicating that no obvious Ru sintering occurs during the reaction. This result can be attributed to the SMSI to suppress particle migration and Ostwald ripening [61]. This Ru particle size is substantially larger than the optimal size of ~ 2 nm, which possesses a maximum density of B_5 step sites (composed of five Ru atoms at the step lattice) responsible for N_2 activation [62]. The relatively large size of Ru nanoparticles is consistent with the limited surface area of the $SrCO_3$ support (6.1 $m^2 \cdot g^{-1}$, Fig. S2 in the ESM). The $SrCO_3$ support was then dispersed by being ball-milled with CNTs, which possess a high specific surface area (120.7 $m^2 \cdot g^{-1}$). After loading Ru, the composite catalyst Ru-$SrCO_3$/CNTs was produced. SEM images (Figs. S12(g)–S12(i) in the ESM) show that CNTs are clearly observed to be interwoven like a spider web across the surface of $SrCO_3$. Notably, the presence of CNTs results in smaller and better-dispersed $SrCO_3$ particles, thereby increasing the specific surface area, enhancing electron transport capability, and reducing Ru particle size, all of which are key structural factors contributing to the enhanced catalytic performance (Fig. 1).

HRTEM images (Figs. 3(a) and 3(b)) reveal that in Ru-$SrCO_3$/CNTs catalysts, Ru nanoparticles (highlighted in red) are mainly anchored around $SrCO_3$ (highlighted in yellow) located on the CNT surface (highlighted in blue). This configuration leads to the formation of Ru-$SrCO_3$ interfaces due to the SMSI between Ru and $SrCO_3$ [39], confirming the stacking structure of $SrCO_3$-supported Ru spread on CNTs. Moreover, the statistical results of Ru particle sizes reveal that the average size of Ru species for Ru-

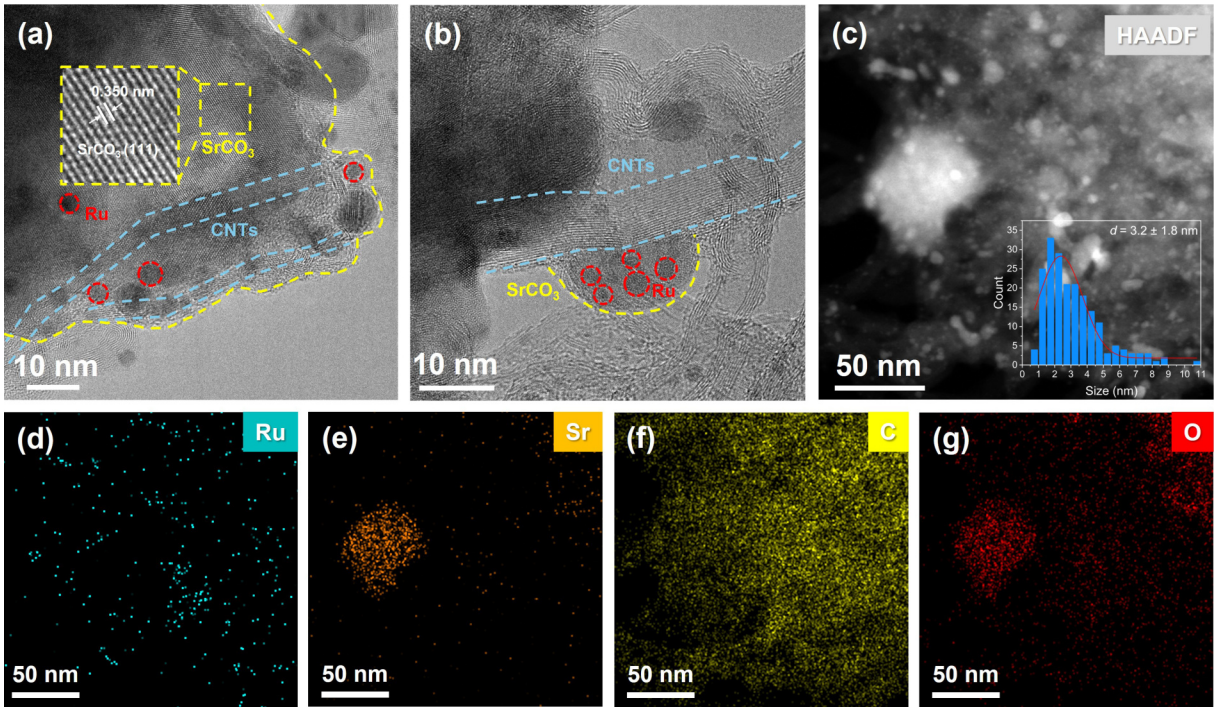

Figure 3 TEM characterization of Ru-$SrCO_3$/CNTs catalysts. ((a) and (b)) HRTEM images of two locations. (c) High-angle annular dark-field scanning transmission electron microscopy (HAADF-STEM) image, with the corresponding size distribution of Ru nanoparticles indicated by the inset. ((d)–(g)) EDS mappings of (d) Ru, (e) Sr, (f) C, and (g) O.

$SrCO_3$/CNTs (3.2 nm) is smaller than that of Ru/$SrCO_3$ (4.3 nm), confirming the enhanced dispersion by CNTs (Fig. 3(c)). In addition, energy dispersive X-ray spectroscopy (EDS) of the used Ru-$SrCO_3$/CNTs catalyst shows a uniform distribution of Ru, Sr, C, and O across the support (Figs. 3(d)–3(g)). This homogeneous elemental dispersion indicates that the highly-active catalyst is also structurally stable during the NH_3 synthesis. Evidently, HRTEM reveals a sub-nanoscale intimate contact among the Ru nanoparticles, $SrCO_3$, and CNTs. Together with our spectroscopic analysis and DFT calculations (below), we propose a "multistage electron-donating model" to describe the interfacial synergy in the K-Ru-$SrCO_3$/CNTs catalyst. Under reaction conditions, the CNTs not only serve as a conductive support but also create a localized carbothermal reduction environment, which facilitates the partial reduction of surface $SrCO_3$ to low-valence Sr species, i.e., essentially Sr^0 atoms. These Sr^0 species, together with the bulk basic $SrCO_3$ and the K promoter, form an integrated electron-donor array. The close contact at the sub-nanometer lattice scale enables efficient electron transfer to the Ru d-orbitals, thereby promoting the polarization and cleavage of the N≡N bond by donating electrons into the antibonding orbitals of N_2 molecules.

3.4 Electronic state

To further evaluate how $SrCO_3$ affects the catalytic activity, we first examined the electronic state of Ru/$SrCO_3$, Ru/CNTs, and Ru-$SrCO_3$/CNTs by using XPS. In Ru 3p XPS spectra (Fig. 4(a)), the binding energy (BE) of Ru^0 over Ru/$SrCO_3$ (462.2 eV) is lower than that of Ru/CNTs (462.3 eV), indicating an increased electron density on the Ru surface, which is further supported by the higher proportion of Ru^0 species (Ru^0/(Ru^0 + $Ru^{\gamma+}$)) in Ru/$SrCO_3$ (91.8%) compared to that in Ru/CNTs (82.4%). These results demonstrate that within the Ru/$SrCO_3$ and Ru/CNTs systems, the $SrCO_3$ support acts as an efficient electron donor for Ru metal and promotes the reduction of Ru species, whereas CNTs do not possess this capability. Moreover, Ru-$SrCO_3$/CNTs exhibits an even lower binding energy of Ru 3p (462.0 eV) than Ru/$SrCO_3$ (462.2 eV), suggesting that CNTs may play another role related to modulating the electronic structure beyond their dispersive function. To verify this hypothesis, Sr 3d XPS spectra over Ru/$SrCO_3$ and Ru-$SrCO_3$/CNTs were recorded and are summarized in Fig. 4(b). For Ru/$SrCO_3$, the binding energies of 133.3 and 135.1 eV can be assigned to $Sr^{\gamma+}$, implying that the $SrCO_3$ support efficiently donates electrons to Ru metal mainly in the form of a compound. Surprisingly, the unexpected Sr^0 (BE = 132.5 and 134.4 eV) besides the anticipated $Sr^{\gamma+}$ (BE = 133.7 and 135.4 eV) is also observed over Ru-$SrCO_3$/CNTs. This result indicates that the surface $SrCO_3$ is partially reduced by CNTs to generate near-metallic Sr^0 species during the reaction, which effectively enhances the electron density on Ru and thereby indirectly boosts the N_2 activation. Meanwhile, the unreduced bulk $SrCO_3$ continues to donate electrons in its compound state, as observed in the Ru/$SrCO_3$ system. In a word, we postulate that $SrCO_3$ acts as an effective electron donor to Ru not only in its compound form but also in a metallic state over Ru-$SrCO_3$/CNTs, thereby achieving highly efficient N_2 activation and NH_3 synthesis. To verify this assumption at the molecular level, we analyzed the Bader charges of Ru in Ru/CNTs and Ru-$SrCO_3$/CNTs (Figs. S18(a) and S18(b) in the ESM). It can be observed that upon the introduction of $SrCO_3$ to Ru/CNTs, the positive charge on Ru_8 decreases from 0.90 |e| to 0.24 |e|, indicating a significant increase in the electron density on Ru surface. Consequently, upon the addition of $SrCO_3$, the adsorption energy of N_2 increases from −0.24 to −0.96 eV (Fig. S18(c) in the ESM), indicating that $SrCO_3$ significantly enhances N_2 adsorption. Correspondingly, the adsorbed N≡N bond length elongates from 1.30 to 1.32 Å, confirming that the electron-donating effect of $SrCO_3$ significantly promotes the adsorption and activation of N_2.

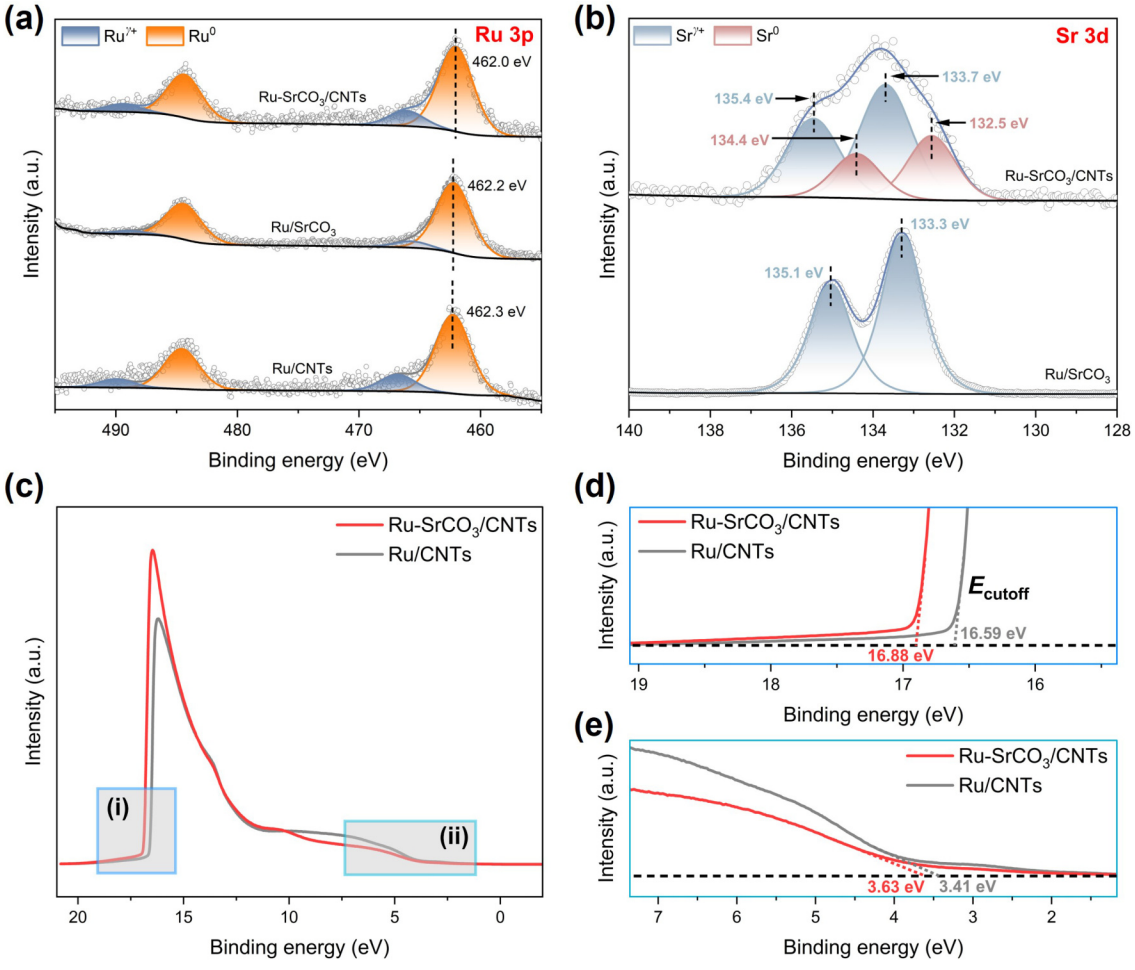

Figure 4 Electronic state characterization. (a) Ru 3p XPS spectra of Ru-$SrCO_3$/CNTs, Ru/$SrCO_3$, and Ru/CNTs catalysts. (b) Sr 3d XPS spectra of Ru-$SrCO_3$/CNTs and Ru/$SrCO_3$ catalysts. (c) UPS spectra over Ru-$SrCO_3$/CNTs and Ru/CNTs catalysts. (d) The magnified images of corresponding area (i) in (c), indicating work function. (e) The magnified images of corresponding area (ii) in (c), indicating d-band center.

This enhancement is attributed to the dual electron-donor effect of $SrCO_3$, which markedly increases the electron density on the Ru surface.

As a complementary technique to XPS, UPS (Fig. 4(c)) provides an independent assessment of the catalysts' electron escape capability, which is directly relevant to their efficacy in activating N_2. Based on the cutoff energy of the secondary electron emission [23], the work function (Φ_{WF}) was calculated using the equation of $\Phi_{WF} = h\nu$ (21.22 eV) − E_{cutoff}. The value for Ru/CNTs is determined to be 4.63 eV, which decreases to 4.34 eV for Ru-$SrCO_3$/CNTs (Fig. 4(d)). A lower work function induced by $SrCO_3$ addition over Ru-$SrCO_3$/CNTs facilitates electron transfer at catalytic interfaces (e.g., Ru-$SrCO_3$), where trapped electrons become more loosely bound. This fact reduces the energy barrier for donating electrons from Ru sites into the anti-bonding π^* orbitals of adsorbed N_2, thereby weakening the N≡N bond and accelerating N_2 dissociation [22]. Such lower work function can be attributed to the excellent electron-donating ability achieved by $SrCO_3$ in two distinct states (e.g., compound and near-metallic). Furthermore, the d-band center (ε_d) values of Ru/CNTs and Ru-$SrCO_3$/CNTs evaluated from magnified images (i) and (ii) were estimated to be 3.41 and 3.63 eV, respectively (Fig. 4(e)). The observed downshift in ε_d for Ru-$SrCO_3$/CNTs indicates a decreased antibonding energy state, which in turn weakens the adsorption of NH_x (x = 0–3) intermediates on Ru sites [63], a change that promotes NH_x desorption and is consistent with the less negative NH_3 reaction orders over $SrCO_3$-supported catalysts. The reduction in work function and downshift of the d-band center, induced by the introduction of $SrCO_3$, create an electronic environment that concurrently favors both N_2 activation and the subsequent desorption of NH_x intermediates, collectively ensuring high-efficiency NH_3 synthesis.

3.5 Understanding of reactant activation

To comprehend the reaction mechanism, the activation of N_2 and H_2 was investigated via *in-situ* characterizations (Fig. 5), such as *in-situ* DRIFTS of CO and N_2 as well as quasi *in-situ* XPS spectra of Ru 3p over Ru/$SrCO_3$ catalysts. As demonstrated in Fig. S19 in the ESM, the strongest absorption peak at 2030 cm^{-1} can be attributed to the linearly-adsorbed CO on Ru B_5 sites [64, 65], indicating the existence of a dissociation mechanism over Ru/$SrCO_3$ catalysts [25]. The subsequent investigation was directed toward studying N_2 adsorption using *in-situ* N_2-DRIFTS, as shown in Fig. 5(a). In contrast to conventional Ru catalysts (e.g., Ru/MgO, 2231 cm^{-1}) [66], Ru/$SrCO_3$ exhibits a peak centered at a much lower wavenumber of approximately 1758 cm^{-1}. To validate whether this peak corresponds to N_2 adsorption, the atmosphere was alternately switched between N_2 and Ar. The reversible disappearance and reappearance of the peak at 1758 cm^{-1} confirm its assignment to N_2

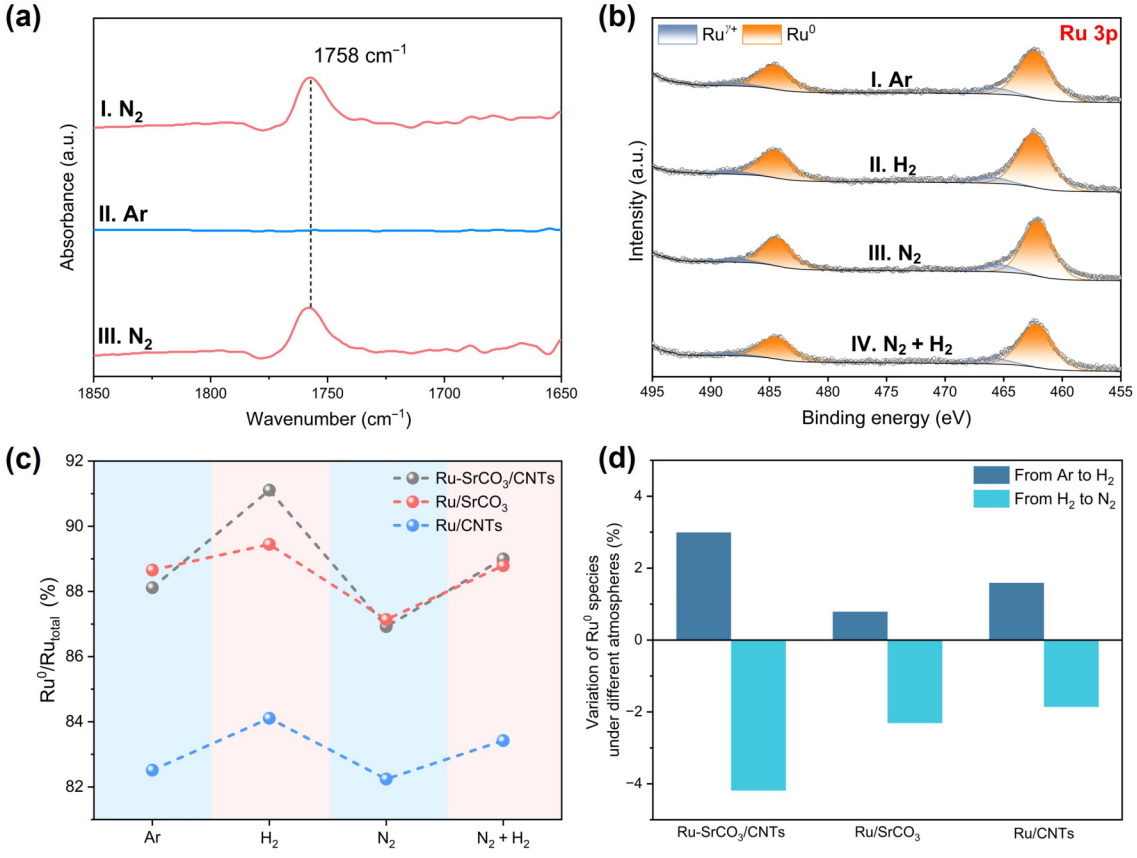

Figure 5 *In-situ* characterizations of reactant activation. (a) *In-situ* N_2 DRIFTS of Ru/$SrCO_3$ catalysts. (b) Quasi *in-situ* XPS spectra of Ru 3p over Ru/$SrCO_3$ catalysts under different reaction atmospheres. (c) Ru^0/Ru_{total} ratio for Ru-$SrCO_3$/CNTs, Ru/$SrCO_3$, and Ru/CNTs catalysts under different atmospheres. (d) Variation of Ru^0 species under different atmospheres.

adsorption. Such red shift of the N_2 adsorption band suggests a significant electron transfer from $SrCO_3$ to Ru sites [67], which is favorable for N_2 activation. This conclusion coincides with the XPS and UPS conclusions in Fig. 4, collectively approving the electron-donating effect of $SrCO_3$.

To elucidate the active sites and reaction mechanism, quasi *in-situ* XPS analysis was performed on Ru/$SrCO_3$, Ru/CNTs, and Ru-$SrCO_3$/CNTs catalysts at 400 °C. The surface state evolution was monitored during sequential exposure to Ar, H_2, N_2, and a 25%N_2-75%H_2 atmosphere, with the raw data presented in Fig. 5(b), and Figs. S20 and S21 in the ESM. Two peaks corresponding to the Ru $3p_{3/2}$ and Ru $3p_{1/2}$ core levels appear at lower binding energies of ca. 462.3 nd 484.5 eV, respectively, which are attributed to Ru^0 species. Two additional peaks at ca. 466.1 and 488.3 eV are assigned to $Ru^{\gamma+}$. The extracted results (Fig. 5(c)) show that the Ru^0 fraction increases for all three catalysts when the atmosphere is switched from Ar to H_2, indicating that some $Ru^{\gamma+}$ species accept electrons from H_2 and are reduced to Ru^0 via the pathway of $Ru^{\gamma+} + H_2 \rightarrow 2^*H + Ru^0$. Conversely, switching the atmosphere from H_2 to N_2 leads to a decrease in the Ru^0 fraction, suggesting that some Ru^0 species are oxidized back to $Ru^{\gamma+}$ species by donating electrons to N_2 via the pathway of $Ru^0 + N_2 \rightarrow {}^*N_2 + Ru^{\gamma+}$. These reversible changes confirm that Ru^0 species serve as the active sites in these catalysts. Moreover, because the variation in Ru^0 fraction responds directly to the reactive gas environment, it can serve as a descriptor for the extent of reactant activation. Specifically, the increase in Ru^0 fraction upon switching from Ar to H_2 reflects the oxidation of H_2, with a larger increase indicating more extensive H_2 activation. Similarly, the decrease in Ru^0 fraction upon switching from H_2 to N_2 reflects the reduction of N_2, with a more pronounced decrease indicating greater N_2 activation. Thus, the change in Ru^0 fraction under different atmospheres acts as a descriptor for reactant activation via the electron transfer effect. On this basis, the variations in Ru^0 fraction across the three catalysts under different atmospheres are summarized in Fig. 5(d). Among them, Ru-$SrCO_3$/CNTs exhibits the largest variation in Ru^0 fractions during both the Ar → H_2 and H_2 → N_2 transitions, confirming its strongest capability for activating H_2 and N_2. This optimal activity over Ru-$SrCO_3$/CNTs catalysts can be attributed to the enhanced electron-donating effect achieved by the introduction of $SrCO_3$, which donates electrons through two distinct pathways, as revealed in Fig. 4.

3.6 Hydrogen poisoning mitigation

Conventional Ru-based catalysts (e.g., Ru/CNTs) suffer from hydrogen poisoning, which is detrimental to NH_3 synthesis under mild conditions [28, 60]. In contrast, $SrCO_3$-supported Ru-based catalysts effectively mitigate this issue indicated by the positive H_2 reaction orders, enabling remarkable NH_3 synthesis. To further understand the unique hydrogen adsorption behavior on this catalyst, WO_3 color change experiments were performed over Ru/CNTs and Ru-$SrCO_3$/CNTs catalysts (Fig. 6). The underlying reason is that pure WO_3 cannot react directly with H_2 at low temperature but only with H atoms to form dark blue H_xWO_3, whereby H atoms are generated from H_2 dissociation on the catalyst surface and then migrate onto the WO_3 support [68]. Consequently, the color change can serve as a direct indicator for

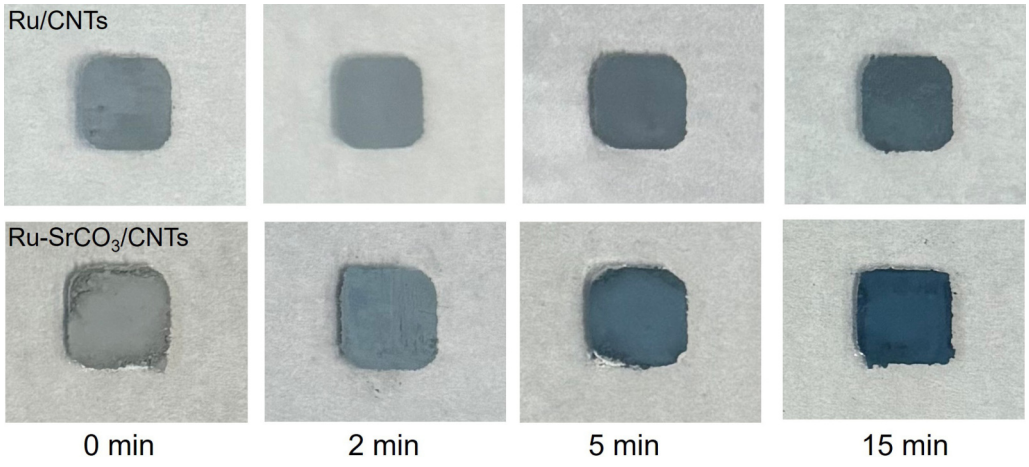

Figure 6 Hydrogen poisoning mitigation. Color change experiments on Ru/CNTs + WO_3 and Ru-$SrCO_3$/CNTs + WO_3 after hydrogen treatment at 200 °C for various time.

evaluating the hydrogen spillover effect [69, 70]. While the H_2–D_2 exchange experiment is commonly used to demonstrate hydrogen dissociation [60], this technique cannot directly confirm hydrogen spillover, the subsequent migration of dissociated hydrogen species from the metal to the support. After H_2 treatment, the mixture of Ru/CNTs and WO_3 turned slightly blue, whereas the Ru-$SrCO_3$/CNTs and WO_3 mixture presented a distinctly darker blue color. This visual contrast thus demonstrates a more pronounced hydrogen spillover effect on the Ru-$SrCO_3$/CNTs catalyst, which is consistent with the positive H_2 reaction orders over $SrCO_3$-supported catalysts. In short, the hydrogen spillover is significantly enhanced by the addition of $SrCO_3$, which accelerates the migration of dissociated *H species away from Ru sites. This rapid removal effectively alleviates hydrogen poisoning over Ru-$SrCO_3$/CNTs. Consequently, a greater number of metallic Ru sites remain available for the adsorption and subsequent dissociation of N_2, which is the key to the improved performance of NH_3 synthesis under mild conditions.

4 Conclusions

In this work, a novel bifunctional support $SrCO_3$ was developed for the thermally catalytic synthesis of NH_3 under mild conditions. Specifically, $SrCO_3$ functions as an excellent electron donor through two distinct pathways, alkaline support itself and near-metallic state generated from reduction of surface $SrCO_3$. Such unique mechanism significantly increases the charge density of Ru sites, thus promoting N_2 activation by boosting charge transfer from Ru atoms to N_2 molecules. Simultaneously, it facilitates NH_x intermediate desorption by downshifting the ε_d and significantly enhances hydrogen spillover to suppress hydrogen poisoning. These synergistic effects endow Ru-$SrCO_3$/CNTs catalyst with superior capabilities for N_2 activation, hydrogen poisoning mitigation, and NH_3 desorption, ultimately leading to its exceptional performance in NH_3 synthesis. Particularly, the K-promoted Ru-$SrCO_3$/CNTs (K-Ru-$SrCO_3$/CNTs) delivers an outstanding NH_3 synthesis rate of 61.6 $mmol_{NH_3} \cdot g_{cat}^{-1} \cdot h^{-1}$ at 400 °C and 0.9 MPa, which is 1.8 times that of K-Ru/CNTs (33.9 $mmol_{NH_3} \cdot g_{cat}^{-1} \cdot h^{-1}$) and ranks among the best reported Ru-based catalysts with loading ≤ 5 wt.%. This work not only extends the application scope of $SrCO_3$, but also opens a new approach to designing efficient catalysts for the mild-condition NH_3 synthesis.

Electronic Supplementary Material: Supplementary material (detailed experimental reagents; XRD, XPS, and TEM characterization data; and N_2 physical adsorption and ICP-OES results) is available in the online version of this article at https://doi.org/10.26599/NR.2026.94908744.

Data availability

All data needed to support the conclusions in the paper are presented in the manuscript and the Electronic Supplementary Material. Additional data related to this paper may be requested from the corresponding author upon request.

Acknowledgements

All authors thank the Seed Foundation of Tianjin University (No. 2025XJ1-0001) and Haihe Laboratory of Sustainable Chemical Transformations (No. 24HHWCSS00009) for the financial support. Our thanks also go to Mr. Kui Lin at Analysis and Testing Center of Tianjin University for the quasi in situ XPS tests.

Declaration of competing interest

All the contributing authors report no conflict of interests in this work.

Author contribution statement

X. H. H.: Data curation, validation, writing manuscript, experimental design. J. K. W.: Data curation, experimental design. Z. L. C.: Data curation, experimental design. H. L. C.: DFT calculation. Y. F. Y.: Data curation. Z. J. S.: Data curation. X. C.: Data curation. L. L. L.: Data curation, experimental design. Y. A. Y.: Project administration, funding acquisition, writing and revising manuscript. All the authors have approved the final manuscript.

Use of AI statement

None.

References

[1] Kumar, N. A.; Dar, M. A.; Gul, R.; Baek, J. B. Graphene and

molybdenum disulfide hybrids: Synthesis and applications. *Mater. Today* **2015**, *18*, 286–298.
[2] Fadai, D.; Esfandabadi, Z. S.; Abbasi, A. Analyzing the causes of non-development of renewable energy-related industries in Iran. *Renew. Sust. Energ. Rev.* **2011**, *15*, 2690–2695.
[3] Gernaat, D. E. H. J.; De Boer, H. S.; Daioglou, V.; Yalew, S. G.; Müller, C.; Van Vuuren, D. P. Climate change impacts on renewable energy supply. *Nat. Clim. Change* **2021**, *11*, 119–125.
[4] Service, R. F. Liquid sunshine. *Science* **2018**, *361*, 120–123.
[5] Guo, J. P.; Chen, P. Catalyst: NH_3 as an energy carrier. *Chem* **2017**, *3*, 709–712.
[6] Tabassum, H.; Guo, W. H.; Meng, W.; Mahmood, A.; Zhao, R.; Wang, Q. F.; Zou, R. Q. Metal-organic frameworks derived cobalt phosphide architecture encapsulated into B/N co-doped graphene nanotubes for all pH value electrochemical hydrogen evolution. *Adv. Energy Mater.* **2017**, *7*, 1601671.
[7] Staffell, I.; Scamman, D.; Velazquez Abad, A.; Balcombe, P.; Dodds, P. E.; Ekins, P.; Shah, N.; Ward, K. R. The role of hydrogen and fuel cells in the global energy system. *Energy Environ. Sci.* **2019**, *12*, 463–491.
[8] Eberle, U.; Felderhoff, M.; Schüth, F. Chemical and physical solutions for hydrogen storage. *Angew. Chem., Int. Ed.* **2009**, *48*, 6608–6630.
[9] Tan, R. K.; Mu, X. W.; Wang, X. H.; Kong, Y. X.; Ji, Q.; Zhan, Q. Y.; Xiong, Q. C.; Li, L. Breakthrough photothermal ammonia decomposition via low-barrier Ni–CeO_{2-x} interfaces on carbon nanotubes. *Nat. Commun.* **2025**, *16*, 11433.
[10] Wang, Q. R.; Guo, J. P.; Chen, P. Recent progress towards mild-condition ammonia synthesis. *J. Energy Chem.* **2019**, *36*, 25–36.
[11] He, T.; Pachfule, P.; Wu, H.; Xu, Q.; Chen, P. Hydrogen carriers. *Nat. Rev. Mater.* **2016**, *1*, 16059.
[12] Erisman, J. W.; Sutton, M. A.; Galloway, J.; Klimont, Z.; Winiwarter, W. How a century of ammonia synthesis changed the world. *Nat. Geosci.* **2008**, *1*, 636–639.
[13] Schüth, F.; Palkovits, R.; Schlögl, R.; Su, D. S. Ammonia as a possible element in an energy infrastructure: catalysts for ammonia decomposition. *Energy Environ. Sci.* **2012**, *5*, 6278–6289.
[14] Ojha, D. K.; Kale, M. J.; McCormick, A. V.; Reese, M.; Malmali, M.; Dauenhauer, P.; Cussler, E. L. Integrated ammonia synthesis and separation. *ACS Sustainable Chem. Eng.* **2019**, *7*, 18785–18792.
[15] Smith, C.; Hill, A. K.; Torrente-Murciano, L. Current and future role of Haber–Bosch ammonia in a carbon-free energy landscape. *Energy Environ. Sci.* **2020**, *13*, 331–344.
[16] Zhang, Y. Y.; Li, J. J.; Cai, J. H.; Yang, L. L.; Zhang, T. H.; Lin, J. X.; Wang, X. Y.; Chen, C. Q.; Zheng, L. R.; Au, C. T. et al. Construction of spatial effect from atomically dispersed Co anchoring on subnanometer Ru cluster for enhanced N_2-to-NH_3 conversion. *ACS Catal.* **2021**, *11*, 4430–4440.
[17] Li, J.; Zhan, G. M.; Yang, J. H.; Quan, F. J.; Mao, C. L.; Liu, Y.; Wang, B.; Lei, F. C.; Li, L. J.; Chan, A. W. M. et al. Efficient ammonia electrosynthesis from nitrate on strained ruthenium nanoclusters. *J. Am. Chem. Soc.* **2020**, *142*, 7036–7046.
[18] Rosowski, F.; Hornung, A.; Hinrichsen, O.; Herein, D.; Muhler, M.; Ertl, G. Ruthenium catalysts for ammonia synthesis at high pressures: Preparation, characterization, and power-law kinetics. *Appl. Catal. A: Gen.* **1997**, *151*, 443–460.
[19] Aika, K. I.; Takano, T.; Murata, S. Preparation and characterization of chlorine-free ruthenium catalysts and the promoter effect in ammonia synthesis: 3. A magnesia-supported ruthenium catalyst. *J. Catal.* **1992**, *136*, 126–140.
[20] Kitano, M.; Inoue, Y.; Ishikawa, H.; Yamagata, K.; Nakao, T.; Tada, T.; Matsuishi, S.; Yokoyama, T.; Hara, M.; Hosono, H. Essential role of hydride ion in ruthenium-based ammonia synthesis catalysts. *Chem. Sci.* **2016**, *7*, 4036–4043.
[21] Kitano, M.; Inoue, Y.; Yamazaki, Y.; Hayashi, F.; Kanbara, S.; Matsuishi, S.; Yokoyama, T.; Kim, S. W.; Hara, M.; Hosono, H. Ammonia synthesis using a stable electride as an electron donor and reversible hydrogen store. *Nat. Chem.* **2012**, *4*, 934–940.
[22] Hattori, M.; Iijima, S.; Nakao, T.; Hosono, H.; Hara, M. Solid solution for catalytic ammonia synthesis from nitrogen and hydrogen gases at 50 °C. *Nat. Commun.* **2020**, *11*, 2001.
[23] Peng, X. B.; Luo, Y. J.; Zhang, T. H.; Deng, J. X.; Zhou, Y. L.; Li, J. X.; Ni, J.; Lin, B. Y.; Lin, J. X.; Wu, D. S. et al. Potassium promoter regulates electronic structure and hydrogen spillover of ultrasmall Ru nanoclusters catalyst for ammonia synthesis. *Chem. Eng. Sci.* **2024**, *292*, 120021.
[24] Shadravan, V.; Cao, A.; Bukas, V. J.; Grønborg, M. K.; Damsgaard, C. D.; Wang, Z. B.; Kibsgaard, J.; Nørskov, J. K.; Chorkendorff, I. Enhanced promotion of Ru-based ammonia catalysts by *in situ* dosing of Cs. *Energy Environ. Sci.* **2022**, *15*, 3310–3320.
[25] Zheng, J. W.; Liao, F. L.; Wu, S.; Jones, G.; Chen, T. Y.; Fellowes, J.; Sudmeier, T.; McPherson, I. J.; Wilkinson, I.; Tsang, S. C. E. Efficient non-dissociative activation of dinitrogen to ammonia over lithium-promoted ruthenium nanoparticles at low pressure. *Angew. Chem., Int. Ed.* **2019**, *58*, 17335–17341.
[26] Cao, A.; Zhang, K.; Vernieres, J.; Wandall, L. H.; Tankard, R. E.; Kibsgaard, J.; Chorkendorff, I.; Nørskov, J. K. The Co/NbN interphase as an effective ammonia synthesis catalyst. *Chem* **2025**, *11*, 102618.
[27] Zhang, K.; Cao, A.; Wandall, L. H.; Vernieres, J.; Kibsgaard, J.; Nørskov, J. K.; Chorkendorff, I. Spin-mediated promotion of Co catalysts for ammonia synthesis. *Science* **2024**, *383*, 1357–1363.
[28] Wu, S.; Peng, Y. K.; Chen, T. Y.; Mo, J. Y.; Large, A.; Mcpherson, I.; Chou, H. L.; Wilkinson, I.; Venturini, F.; Grinter, D. et al. Removal of hydrogen poisoning by electrostatically polar MgO support for low-pressure NH_3 synthesis at a high rate over the Ru catalyst. *ACS Catal.* **2020**, *10*, 5614–5622.
[29] Li, L. L.; Jiang, Y. F.; Zhang, T. H.; Cai, H. F.; Zhou, Y. L.; Lin, B. Y.; Lin, X. Y.; Zheng, Y.; Zheng, L. R.; Wang, X. Y. et al. Size sensitivity of supported Ru catalysts for ammonia synthesis: From nanoparticles to subnanometric clusters and atomic clusters. *Chem* **2022**, *8*, 749–768.
[30] Hara, M.; Kitano, M.; Hosono, H. Ru-loaded C12A7:e^- electride as a catalyst for ammonia synthesis. *ACS Catal.* **2017**, *7*, 2313–2324.
[31] Baik, Y.; Chi, S.; Lee, K.; Oh, D.; Lee, K.; Choi, M. Electron and proton storage on separate Ru and BaO domains mediated by conductive low-work-function carbon to accelerate ammonia synthesis. *Nat. Catal.* **2025**, *8*, 248–256.
[32] Baik, Y.; Kwen, M.; Lee, K.; Chi, S.; Lee, S.; Cho, K.; Kim, H.; Choi, M. Splitting of hydrogen atoms into proton-electron pairs at BaO–Ru interfaces for promoting ammonia synthesis under mild conditions. *J. Am. Chem. Soc.* **2023**, *145*, 11364–11374.
[33] Rossetti, I.; Pernicone, N.; Forni, L. Promoters effect in Ru/C ammonia synthesis catalyst. *Appl. Catal. A: Gen.* **2001**, *208*, 271–278.
[34] Li, Z. C.; Lu, Y. F.; Li, J.; Xu, M.; Qi, Y. P.; Park, S. W.; Kitano, M.; Hosono, H.; Chen, J. S.; Ye, T. N. Multiple reaction pathway on alkaline earth imide supported catalysts for efficient ammonia synthesis. *Nat. Commun.* **2023**, *14*, 6373.
[35] Huang, J.; Yuan, M. W.; Li, X. Z.; Wang, Y.; Li, M. W.; Li, J. J.; You, Z. X. Inhibited hydrogen poisoning for enhanced activity of promoters-Ru/$Sr_2Ta_2O_7$ nanowires for ammonia synthesis. *J. Catal.* **2020**, *389*, 556–565.
[36] Horiuchi, Y.; Kamei, G.; Saito, M.; Matsuoka, M. Development of ruthenium-loaded alkaline-earth titanates as catalysts for ammonia synthesis. *Chem. Lett.* **2013**, *42*, 1282–1284.
[37] Peng, X. B.; Chen, X. C.; Zhou, Y. L.; Sun, F. X.; Zhang, T. H.; Zheng, L. R.; Jiang, L. L.; Wang, X. Y. Size-dependent activity of supported Ru catalysts for ammonia synthesis at mild conditions. *J. Catal.* **2022**, *408*, 98–108.
[38] Chen, C. Q.; Wu, K.; Ren, H. J.; Zhou, C.; Luo, Y.; Lin, L.; Au, C.; Jiang, L. L. Ru-based catalysts for ammonia decomposition: A mini-review. *Energy Fuels* **2021**, *35*, 11693–11706.
[39] Luo, Z. X.; Zhao, G. Q.; Pan, H. G.; Sun, W. P. Strong metal–support

interaction in heterogeneous catalysts. *Adv. Energy Mater.* **2022**, *12*, 2201395.
[40] Yang, S. X.; Qiao, Y.; He, P.; Liu, Y. J.; Cheng, Z.; Zhu, J. J.; Zhou, H. S. A reversible lithium-CO_2 battery with Ru nanoparticles as a cathode catalyst. *Energy Environ. Sci.* **2017**, *10*, 972–978.
[41] Larichev, Y. V.; Moroz, B. L.; Zaikovskii, V. I.; Yunusov, S. M.; Kalyuzhnaya, E. S.; Shur, V. B.; Bukhtiyarov, V. I. XPS and TEM studies on the role of the support and alkali promoter in Ru/MgO and Ru-Cs^+/MgO catalysts for ammonia synthesis. *J. Phys. Chem. C* **2007**, *111*, 9427–9436.
[42] Zhou, Y. L.; Yang, B.; Wang, L.; Su, K. L.; Liu, B.; Fang, H. P.; Yue, K. X.; Wang, X. Y.; Qi, H. F.; Zheng, L. R. et al. Ru single atom and nanoparticle tandem catalyst unlocking high-efficiency ammonia synthesis under mild conditions. *J. Am. Chem. Soc.* **2025**, *147*, 31136–31146.
[43] Aika, K.; Kumasaka, M.; Oma, T.; Kato, O.; Matsuda, H.; Watanabe, N.; Yamazaki, K.; Ozaki, A.; Onishi, T. Support and promoter effect of ruthenium catalyst. III. Kinetics of ammonia synthesis over various Ru catalysts. *Appl. Catal.* **1986**, *28*, 57–68.
[44] Kresse, G.; Furthmüller, J. Efficient iterative schemes for *ab initio* total-energy calculations using a plane-wave basis set. *Phys. Rev. B* **1996**, *54*, 11169–11186.
[45] Kresse, G.; Furthmüller, J. Efficiency of *ab-initio* total energy calculations for metals and semiconductors using a plane-wave basis set. *Comput. Mater. Sci.* **1996**, *6*, 15–50.
[46] Blöchl, P. E. Projector augmented-wave method. *Phys. Rev. B* **1994**, *50*, 17953–17979.
[47] Perdew, J. P.; Burke, K.; Ernzerhof, M. Generalized gradient approximation made simple. *Phys. Rev. Lett.* **1996**, *77*, 3865–3868.
[48] Perdew, J. P.; Wang, Y. Accurate and simple analytic representation of the electron-gas correlation energy. *Phys. Rev. B* **1992**, *45*, 13244–13249.
[49] Morales, D. M.; Jambrec, D.; Kazakova, M. A.; Braun, M.; Sikdar, N.; Koul, A.; Brix, A. C.; Seisel, S.; Andronescu, C.; Schuhmann, W. Electrocatalytic conversion of glycerol to oxalate on Ni oxide nanoparticles-modified oxidized multiwalled carbon nanotubes. *ACS Catal.* **2022**, *12*, 982–992.
[50] Lv, L. K.; Chu, P. Q.; Han, T.; Jiang, Y. P.; Wang, Z. W.; Liu, Y. X.; Dai, H. X.; Wei, L.; Deng, J. G. Carbon and oxygen double defects-enhanced Ru-based catalyst for ammonia decomposition. *Angew. Chem., Int. Ed.* **2025**, *64*, e202501898.
[51] Aika, K. I.; Hori, H.; Ozaki, A. Activation of nitrogen by alkali metal promoted transition metal I. Ammonia synthesis over ruthenium promoted by alkali metal. *J. Catal.* **1972**, *27*, 424–431.
[52] Jacobsen, C. J. H. Boron nitride: A novel support for ruthenium-based ammonia synthesis catalysts. *J. Catal.* **2001**, *200*, 1–3.
[53] Fu, Q. J.; Wang, X.; Fu, G.; Zheng, N. F.; Qin, R. X. The critical roles of promoters in heterogeneous catalytic hydrogenation. *ACS Catal.* **2026**, *16*, 1894–1928.
[54] Hansen, T. W.; Wagner, J. B.; Hansen, P. L.; Dahl, S.; Topsøe, H.; Jacobsen, C. J. H. Atomic-resolution *in situ* transmission electron microscopy of a promoter of a heterogeneous catalyst. *Science* **2001**, *294*, 1508–1510.
[55] Cao, A.; Bukas, V. J.; Shadravan, V.; Wang, Z. B.; Li, H.; Kibsgaard, J.; Chorkendorff, I.; Nørskov, J. K. A spin promotion effect in catalytic ammonia synthesis. *Nat. Commun.* **2022**, *13*, 2382.
[56] Mao, C. L.; Yu, L. H.; Li, J.; Zhao, J. C.; Zhang, L. Z. Energy-confined solar thermal ammonia synthesis with K/Ru/$TiO_{2-x}H_x$. *Appl. Catal. B: Environ.* **2018**, *224*, 612–620.
[57] Ye, T. N.; Park, S. W.; Lu, Y. F.; Li, J.; Sasase, M.; Kitano, M.; Tada, T.; Hosono, H. Vacancy-enabled N_2 activation for ammonia synthesis on an Ni-loaded catalyst. *Nature* **2020**, *583*, 391–395.
[58] Ye, T. N.; Park, S. W.; Lu, Y. F.; Li, J.; Wu, J. Z.; Sasase, M.; Kitano, M.; Hosono, H. Dissociative and associative concerted mechanism for ammonia synthesis over Co-based catalyst. *J. Am. Chem. Soc.* **2021**, *143*, 12857–12866.
[59] Kitano, M.; Kanbara, S.; Inoue, Y.; Kuganathan, N.; Sushko, P. V.; Yokoyama, T.; Hara, M.; Hosono, H. Electride support boosts nitrogen dissociation over ruthenium catalyst and shifts the bottleneck in ammonia synthesis. *Nat. Commun.* **2015**, *6*, 6731.
[60] Zhang, Y. Y.; Peng, X. B.; Tian, H. R.; Yang, B.; Chen, Z. C.; Li, J. J.; Zhang, T. H.; Zhang, M. Y.; Liang, X. C.; Yu, Z. Y. et al. Fullerene on non-iron cluster-matrix co-catalysts promotes collaborative H_2 and N_2 activation for ammonia synthesis. *Nat. Chem.* **2024**, *16*, 1781–1787.
[61] Hu, S. L.; Li, W. X. Sabatier principle of metal–support interaction for design of ultrastable metal nanocatalysts. *Science* **2021**, *374*, 1360–1365.
[62] Honkala, K.; Hellman, A.; Remediakis, I. N.; Logadottir, A.; Carlsson, A.; Dahl, S.; Christensen, C. H.; Nørskov, J. K. Ammonia synthesis from first-principles calculations. *Science* **2005**, *307*, 555–558.
[63] Peng, X. B.; Hu, X. H.; Mao, R. S.; An, M. Q.; Li, J. X.; Zhang, Y. Y.; Zhang, T. H.; Chen, M.; Zhou, Y. L.; Ni, J. et al. Electronic interactions and hydrogen migration over C_{60}-modified Ru catalyst enhance ammonia synthesis. *Chin. Chem. Lett.* **2026**, *37*, 111820.
[64] Feng, J.; Liu, L.; Zhang, X. L.; Wang, J. M.; Ju, X. H.; Li, R. L.; Guo, J. P.; He, T.; Chen, P. Ru nanoparticles on $Y_2O_3$with enhanced metal–support interactions for efficient ammonia synthesis. *Catal. Sci. Technol.* **2023**, *13*, 844–853.
[65] Chin, S. Y.; Williams, C. T.; Amiridis, M. D. FTIR studies of CO adsorption on Al_2O_3- and SiO_2-supported Ru catalysts. *J. Phys. Chem. B* **2006**, *110*, 871–882.
[66] Kubota, J.; Aika, K. I. Infrared studies of adsorbed dinitrogen on supported ruthenium catalysts for ammonia synthesis: Effects of the alumina and magnesia supports and the cesium compound promoter. *J. Phys. Chem.* **1994**, *98*, 11293–11300.
[67] Zhang, Z. J.; Miyashita, K.; Wu, T.; Kujirai, J.; Ogasawara, K.; Li, J.; Jiang, Y. H.; Miyazaki, M.; Matsuishi, S.; Sasase, M. et al. Anion vacancies activate N_2 to ammonia on Ba-Si orthosilicate oxynitride-hydride. *Nat. Chem.* **2025**, *17*, 679–687.
[68] Wang, S.; Lv, Y. P.; Wang, X. L.; Gao, D. W.; Duan, A. J.; Zhao, H. Q.; Zheng, P.; Chen, G. Z. Insights into the active sites of dual-zone synergistic catalysts for semi-hydrogenation under hydrogen spillover. *AIChE J.* **2023**, *69*, e17886.
[69] Xiong, M.; Gao, Z.; Zhao, P.; Wang, G. F.; Yan, W. J.; Xing, S. F.; Wang, P. F.; Ma, J. Y.; Jiang, Z.; Liu, X. C. et al. *In situ* tuning of electronic structure of catalysts using controllable hydrogen spillover for enhanced selectivity. *Nat. Commun.* **2020**, *11*, 4773.
[70] Khoobiar, S. Particle to particle migration of hydrogen atoms on platinum-alumina catalysts from particle to neighboring particles. *J. Phys. Chem.* **1964**, *68*, 411–412.